KINETIC MODELING OF GOLD NANOPARTICLE FORMATION FOR RADIATION DOSE PREDICTION

by

Burak Akar

A thesis submitted in partial fulfillment
of the requirements for the degree

of

Master of Science

in

Chemical Engineering

MONTANA STATE UNIVERSITY
Bozeman, Montana

May 2017

ACKNOWLEDGEMENTS

I would first like to thank my thesis advisor Professor Jeff Heys of the Chemical & Biological Engineering Department at Montana State University. The door to Prof. Heys was always accessible whenever I ran into a trouble spot or had a question about my research or writing.

I would also like to acknowledge by Professor Kaushal Rege and Karthik Subramaniam Pushpavanam of the Chemical Engineering at Arizona State University. They conducted the gold nanoparticle synthesis under ionizing radiation experiments and provided the experimental measurements that are used in this thesis.

Burak Akar

TABLE OF CONTENTS

LIST OF FIGURES

Figure Page

ABSTRACT

Nanoparticles have numerous uses in the biomedical sciences, and this study focused on use of gold nanoparticles (GNPs) for measuring ionizing radiation dose. GNPs synthesized at various radiation doses were experimentally characterized and two mathematical models were developed to simulate the synthesis process. The first is based on the Finke-Watzky model and predicts the rate of soluble gold salt conversion to GNPs, and the second model is based on a population balance model and predicts nanoparticle concentration and size distribution. The model parameters that provided an optimal fit to experimentally gathered data were determined, and both models were able to capture the experimental absorbance time trends. The population balance model, however, had the greater predictive power as it was able to capture mean particle size trends that were consistent with experimental measurement.

CHAPTER ONE: INTRODUCTION

Gold Nanoparticles

Nanoparticles have unique magnetic, optical, electronic, and catalytic properties, which are related to their size and are different from the bulk material properties. Colloidal suspensions of gold nanoparticles can display vibrant colors because gold nanoparticles absorb and scatter light with incredible efficiency [1]. The solutions usually have a red or blue/purple color based on particle size, shape and the local refractive index. They have been used by artists for centuries. Gold and silver nanoparticles were used to make the dichroic glass of the 4th-century Lycurgus Cup, which shows a different color depending on whether or not light is passing through it; red when lit from behind and green when lit from in front [2]. The process that was used to synthesize the nanoparticles or the dichroic glass is not known, and the nanoparticles could even be an accidental or unknown addition to the glass. Such an accidental discovery led to Michael Faraday making some of the first scientific observations about gold nanoparticles. In 1856, Faraday accidentally created a ruby red solution while mounting pieces of gold leaf onto microscope slides. Faraday started to further investigate the optical properties of the colloidal gold. He prepared the first pure sample of colloidal gold and noted the light scattering properties of suspended gold particles, which is now called the Faraday-Tyndall effect [3].

Advanced microscopy methods, such as atomic force microscopy and electron microscopy, have accelerated studies on gold nanoparticles. They were the subject of several biomedical studies because many traditional biological probes such as antibodies, lectins, superantigens, glycans, nucleic acids, and receptors can be attached to colloidal gold particles [4]. There are now many potential innovative applications in numerous fields such as biomedicine [5], electronics [6], catalysis [7], fuel cells [8], magnetic data storage [9], agriculture [10], and solar cells [11].

Most gold nanoparticle synthesis methods involve reduction of chloroauric acid ($H[AuCl_4]$). Generally, a reducing agent is used on a solution of chloroauric acid to reduce Au^{3+} ions to Au^{+} ions, which further reduce to Au^{0} atoms. The Au^{0} atoms are significantly less soluble in aqueous solution, and they act as sites for the reduction of more ions and they combine to form the first stable nuclei. Some sort of stabilizing agent or a capping ligand that sticks to the nanoparticle surface is usually added to prevent the particles from aggregating and to limit their growth. This synthesis was pioneered by J. Turkevich [12], and his methods involved the reaction of small amounts of hot chloroauric acid with small amounts of sodium citrate solution. The colloidal gold was formed because the citrate ions act as both a reducing agent and a capping agent [13]. The method was refined by G. Frens but is still called the Turkevich method [14]. Most synthesis methods follow a similar recipe to the Turkevich method but use different reducing and capping agents as necessary to refine the synthesis process and produce particles of different sizes and shapes [15, 16]. The gold solution can also be reduced using radiolysis or gamma-irradiation [17, 18], potentially allowing the formation of gold

nanoparticles to be used for radiation detection and dosage measurement under the proper conditions.

Radiation Detection

Ionizing radiation has several applications in nuclear power, medical imaging, astrophysics, and medical therapy. When applied in a controlled fashion, ionizing radiation can sterilize various products, including food produce, and kill cancer cells [19]. When released in uncontrolled fashion, ionizing radiation can induce either acute or chronic reactions, it can cause harmful tissue reactions due to cells malfunctioning/dying, cancerous tissue growth and, heritable diseases [20]. Given the potential benefits and harms of using ionizing radiation, reliable and sensitive radiation detection is a key component of harnessing the power and potential of ionizing radiation safely. Since ionizing radiation can induce gold nanoparticle synthesis in a gold salt solution, which causes a visible color change, such a solution could be used to detect and measure radiation dose.

Currently there are a number of radiation dosimeters, available for detecting the radiation exposure during medical and industrial processes. Electronic personal dosimeters (EPD) are a common type of personal dosimeters for ionizing radiation, and they can provide a live readout of radiation dose accumulation and sound alarms at previously determined doses [21]. While they are useful in high dose areas, they can be quite expensive. Another common device is the film badge dosimeter, but it is single use only and uses a radiation sensitive silver film emulsion [22]. Though other dosimeter

materials that are less energy dependent and can more accurately assess radiation dose from a variety of radiation fields with higher accuracy are available, film dosimeters are still in use worldwide. Existing detection methods suffer from a number of limitations, including difficulty of fabrication, high cost, low range of detection, and poor sensitivity. Furthermore, these systems require secondary detection methods in several cases. For example, film dosimeters require either densitometry or spectrophotometry to obtain quantitative measurement of the doses [23, 24].

A detection method that uses a clearly visible color change in response to ionizing radiation would be very useful in many fields since it does not require secondary analyses. Existing colorimetric systems are based on several principles related to radiation-induced chemical reactions and include Fricke or Fricke-like systems, which are based on either oxidation or reduction metal ions, poly(methyl methacrylate) systems (PMMA), and radiochromic dyes [23]. Fricke-like systems have detectable ranges from 1 to several hundred Grays, but typically require spectrophotometry for reading out the chemical changes [23]. PMMA-based systems are excellent high-dose dosimeters with ranges of 10^2 to 10^4 Gy [23]. Radiochromic dyes can be quite sensitive at detecting doses from 10^{-1} up to 10^4, depending on dye species [23]. However, radiochromic dyes are limited by their sensitivity to UV light as well as humidity [23]. Gold nanoparticle synthesis through ionizing radiation can produce color change, thus solutions of gold ions and templating agents can be used as colorimetric radiation detection systems. Figure 1 shows the effects of the templating agent and radiation dose on nanoparticle synthesis rate.

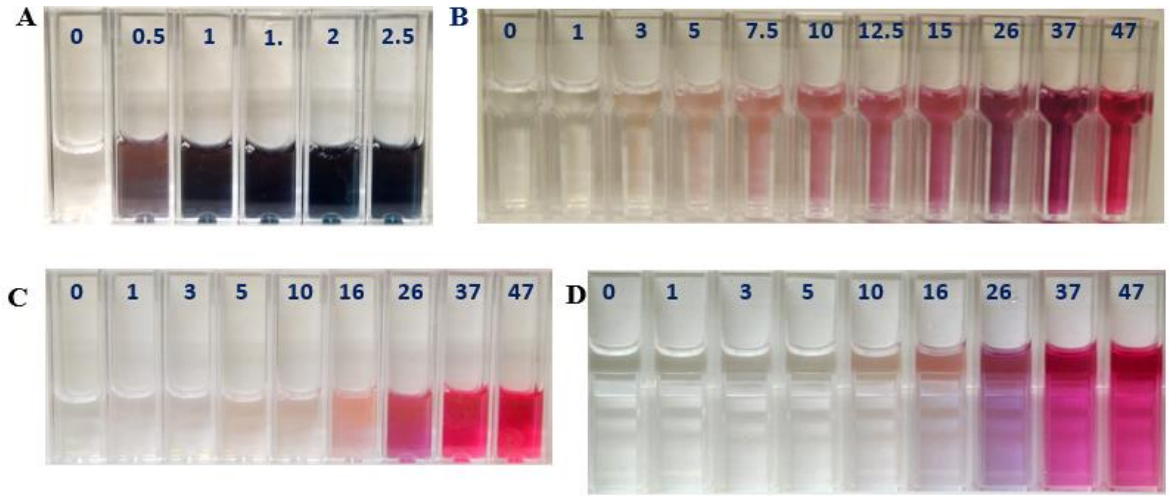

Figure 1. Optical images of samples containing gold ions and different concentrations of templating agents (C_{16}TAB) irradiated with a range of X-ray doses (Gy) (A) 2 mM, (B) 4mM, (C) 10mM, (D) 20mM, 2 hours post X-ray irradiation. The corresponding X-ray radiation dose leading to the observed visual color change is indicated over each sample in Gray (Gy).

Established Kinetic Models for Nanoparticle Formation

In order to produce a reliable dosimeter that utilizes nanoparticle formation, an investigation of factors influencing nanoparticle formation is necessary. A large number of factors such as the templating molecule, radiation dose, and initial soluble gold concentration affect nanoparticle formation. A mathematical framework would enhance the fundamental understanding of the mechanisms controlling nanoparticle formation and, therefore, the efficacy of nano-bio sensing. A mathematical model would also permit the investigation and optimization of parameters that enhance the sensitivity to ionizing radiation, thus reducing the overall experimental burden.

The formation of nanoparticles is generally considered to be a two-step process consisting of nucleation and growth. For many years, the process of the nucleation of nanoparticles has been described through the LaMer burst nucleation, where the monomer undergoes “burst nucleation”, the concentration of free monomers in the solution decreases and nuclei are formed. The rate of this reaction is “effectively infinite” and the reaction stops when the free monomer concentration gets too low [25-27]. While this mechanism accounted for nucleation, growth was explained by Ostwald ripening or particle coalescence. Ostwald ripening was first observed in 1900. The smaller particles within the solution have higher a solubility and surface energy, and these particles dissolve; in turn, allowing the larger particles to grow even more. The mathematical theory of Ostwald ripening within a closed system is described by Lifshitz, Slyozov and Wagner, the LSW theory [28, 29]. Digestive ripening is effectively the inverse of Ostwald ripening. In this case, smaller particles grow at the expense of the larger ones. This effect can also be influential in nanoparticle growth and has been described by Lee et al. [27, 30]. Another way for the nuclei to grow is through collisions and coalescing with other nuclei or clusters.

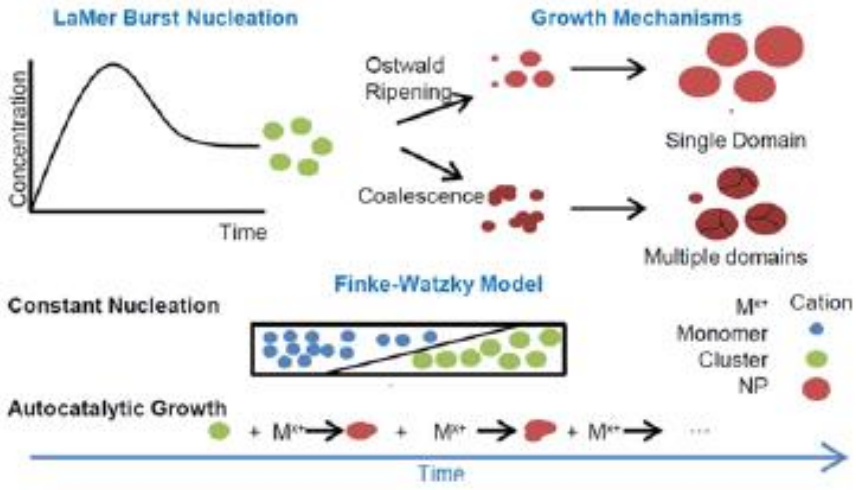

Figure 2. The differences between LaMer Burst Nucleation and the Finke-Watzky Model [27].

LaMer nucleation, coupled with Ostwald ripening and particles coalescing was considered as the only mechanism of nanoparticle growth until Watzky and Finke formulated an approach where both steps happen simultaneously [31]. The first step is a slow continuous nucleation, Eq 1, and the second step is the autocatalytic surface growth, which is frequently assumed to not be diffusion controlled, Eq 2.

$$A \rightarrow B \qquad \text{Eq1}$$

$$A + B \rightarrow 2B \qquad \text{Eq2}$$

Originally, the potential of the method was shown through the kinetic fitting of cyclohexene reduction, but it has not been proven explicitly [27]. Although this method is different from classical nucleation, the nucleation step still requires a critical size described within a classical nucleation framework. This has been shown to be a good fit

for many systems including iridium [32], [33], platinum [34], ruthenium [35] and rhodium [35].

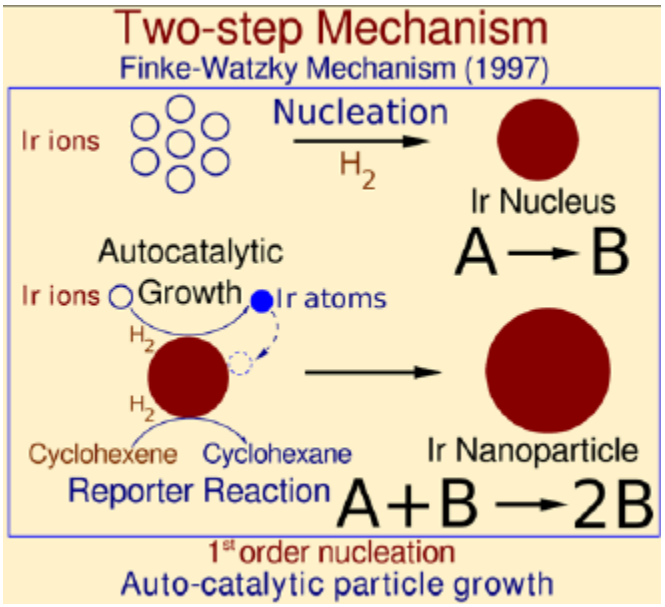

Figure 3. The Two step Finke-Watzky mechanism [36].

There have been several studies on the Finke-Watzky model. Georgiev et al. explored the use of atomic force microscopy (AFM) for examining gold nanoparticle growth [32]. The gold nanoparticles were obtained using Turkevich synthesis at two different temperatures. AFM images taken during growth were analyzed to obtain nanoparticle sizes and to compare the data with dynamic light scattering and transmission electron microscopy measurements. They used a two-step Finke-Watzky kinetic model to fit their spectroscopy data and calculated the corresponding kinetic constants for chemically synthesized gold nanoparticles [32].

The Perala study examined the two-step mechanism for iridium nanoparticles. It expands on the Finke-Watzky mechanism to produce several population balance models (PBM) that predict particle size based on different assumptions about the formation process [36]. Their first population balance model makes the assumption that the growth rate is proportional to particle volume, but their results are more polydisperse than desired. In their experiments, they found that nucleation becomes negligible after the initial induction period, which results in a very monodisperse population. Their second PBM aimed at challenging one of their initial assumptions, and this time they assumed that the growth rate was proportional to surface area. The polydispersity of the modeled result did not improve, unfortunately. They note that one of the ways to make nucleation a negligible process while particle growth continues is to make the former depend on another species. They divided the nucleation step into two steps in order to simulate an intermediate species. They created two more PBMs that tested this alternative synthesis route, the second one assumed second-order dependence on the intermediate species. The new models still did not predict the polydispersity adequately well, and the precursor consumption did not fit as well anymore. However, their analysis of those models revealed that a mechanism that seeks to explain their experimental observations must decrease the time window over which nucleation occurs, by delaying the onset of nucleation. They used a form already available in the literature for nucleation rate with delayed onset of nucleation [36, 37]. Their final model predicts the observed nucleation window correctly. They conclude that the two step mechanism does not capture particle synthesis correctly and out of all the models they investigated, the delayed onset of

nucleation model was the only one that could explain all of the experimental observations consistently [36].

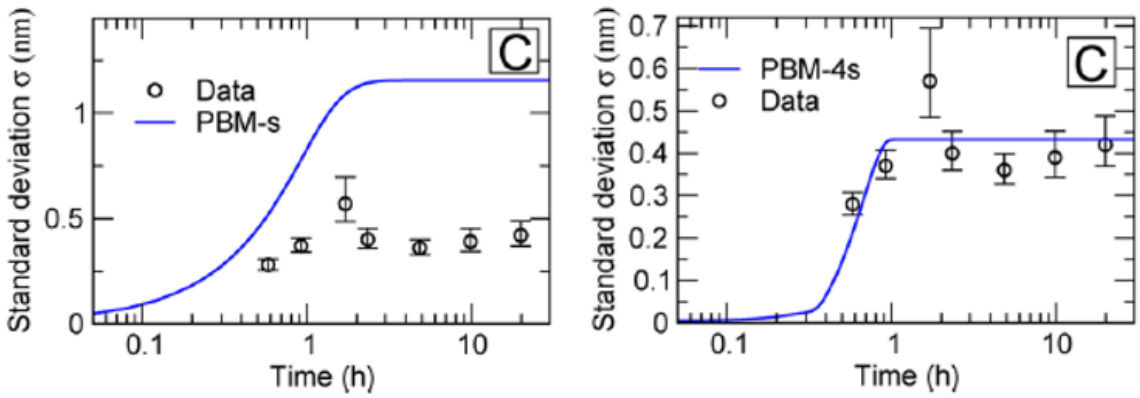

Figure 4. The standard deviation of particle sizes for the first Perala PBM(left) is not aligned with the experimental observations. The fourth Perala PBM(right) fits the data much better [36].

There are also models that do not use the two-step mechanism. Thomas et al. created a mathematical model of the growth kinetics of gold nanorods grown via seed mediated synthesis [38]. They could simplify their models significantly because they had no need for a nucleation step and they assumed that secondary nucleation was impossible, which meant their particle number was constant throughout the simulation. Since they were modeling nanorods, the particles were limited by capping agents and could only grow in one dimension, so they modeled the growth of particles using surface diffusion and mass transfer in one dimension. Although they note that their model could be modified to be used with any seed mediated process.

CHAPTER TWO: METHODS FOR MODELING GNP FORMATION

Gold nanoparticles were synthesized at various radiation doses and the absorbance and mean particle size were measured. The analysis of the measurements showed that as the radiation dose increased, the concentration of synthesized GNPs increased and the diameter of GNPs decreased. Because of the extremely short time scale of the water radiolysis and gold ion reduction reactions, the reduction reactions are not included explicitly in either of the mathematical models described below, and, instead, the initial concentration of zero valence gold atoms is calculated using experimental measurements of absorbance and particle size at different radiation doses. All models assume that Ostwald ripening, digestive ripening and collisions with other particles have negligible effects on particle growth. Two different mathematical models are examined here that predict the formation of GNPs at low radiation doses such as those needed for practical radiation dose measurement.

The Finke-Watzky Model

The first kinetic model describing the formation of gold nanoparticles begins with a reaction describing the formation of stable gold nanoparticle nuclei:

$$A \xrightarrow{k_1} B \qquad \text{Eq.3}$$

where A is the concentration of gold atoms, B represents the total amount of gold in relatively stable nanoparticle nuclei and k_1 is the forward rate of nanoparticle nuclei

formation. The stable nuclei formation step is often the slow step in nanoparticle synthesis. The second reaction in the Finke-Watzky model describes the growth of stable nuclei through the incorporation of additional gold atoms:

$$A + B \overset{k_2}{\rightarrow} 2B. \qquad \text{Eq.4}$$

The Finke-Watzky model ultimately predicts the rate at which insoluble gold atoms, A, are assimilated into gold nanoparticles, B. However, a significant limitation of the Finke-Watzky model is that it does not predict either nanoparticle size or the concentration of particles.

The main prediction of the model, the total moles of gold atoms cumulatively contained in all the particles as a function of time, is converted to an estimate of absorbance using experimental measurements of average particle size so that the model prediction can be compared with the experimental measurements taken using UV-vis spectrometry. The following equation (Beer's Law) was used to convert the model prediction of particle concentration to absorbance [39]:

$$A = \varepsilon b C \qquad \text{Eq.5}$$

where, b is path length (i.e., the distance of the path that the light travels through the sample), ε is the extinction coefficient, and C is the particle concentration. The particle

concentration was calculated by dividing the total concentration of gold atoms in particle form by the mean particle volume:

$$C = \frac{B}{\frac{4}{3}\pi r^3 N_A M_{Au}} \qquad \text{Eq.6}$$

where, N_A is the Avogadro's number and M_{Au} is the molar density of gold, 98 $\frac{mol}{L}$. The diameters of the nanoparticles synthesized under different radiations were measured experimentally, and for the Finke-Watzky model, all synthesized particles were assumed to be the measured mean particle size. The extinction coefficient is also dependent on the particle size and is calculated using:

$$\ln \varepsilon = k * \ln D + a \qquad \text{Eq.7}$$

where, D is the particle diameter and, k and a are constants that were calculated previously to be 3.32111 and 10.80505 for gold nanoparticles [39].

The Population Balance Model

Population balance models explicitly model particles of different sizes and allow prediction of growth based on size. The governing population balance equation is given by:

$$\frac{\partial B(r)}{\partial t} + \frac{\partial}{\partial r}[\mu(r)B(r)] = N \cdot \delta(r - r_c) \qquad \text{Eq.8}$$

where $B(r)$ is the population of particles of size r, $\mu(r)$ is the growth rate for particles of size r, and N is the nucleation rate of particles of critical radius size, r_c. The implementation of particle balance models is frequently achieved by discretizing particles of different sizes into different size groups with each group representing a specific radius range. As a result, nanoparticle growth is split into numerous reactions that each describe the growth of particles in radius range i and, after sufficient time, these particles grow into radius range $i + 1$. In other words, when the particles reach a certain size, they move into a grouping of larger sized particles. Population balance models use the following reactions for nucleation and growth after discretizing particles into various size groups:

$$A \xrightarrow{k_1} B_0 \qquad \text{Nucleation} \qquad \text{Eq.9}$$

$$A + B_i \xrightarrow{k_{2,i}} B_{i+1} \qquad \text{Growth} \qquad \text{Eq.10}$$

where, B_0 is the concentration of stable gold nanoparticle nuclei and B_i is the concentration of nanoparticles in size range i. The smallest stable nuclei (B_0) are assumed to consist of approximately 20 atoms [36], which is used to calculate the minimum radius of the particles. The maximum particle radius is estimated from experimental measurements, and the range of possible particle radii is divided into N discrete groups. The growth reaction leads to particles of slightly larger size, and particles continue to grow at different rates (given below) until the maximum particle radius of 69 nm is reached (N = 50 for current model). A critical issue associated with population balance models is the determination of the growth rate, $k_{2,i}$, which is often a function of particle size.

Material balances on the nucleation and growth reactions result in a model consisting of the following system of differential equations:

$$\frac{dA}{dt} = -k_1 \cdot A^n - \sum_{i=0}^{N-1} k_{2,i} \cdot A \cdot B_i \qquad \text{Eq.11}$$

$$\frac{dB_0}{dt} = k_1 \cdot A^n - k_{2,0} * A \cdot B_0 \qquad \text{Eq.12}$$

$$\frac{dB_i}{dt} = k_{2,i-1} \cdot A \cdot B_{i-1} - k_{2,i} \cdot A \cdot B_i \qquad \text{for } i = 0, 1, \dots, N \qquad \text{Eq.13}$$

$$\frac{dB_N}{dt} = k_{2,N-1} \cdot A \cdot B_{N-1} \qquad \text{Eq.14}$$

The exponent, n, is an unknown parameter that will be determined using the experimental data. Mathematical models of similar systems have used $n = 1$ to 4 [40].

Therefore, values over that range are initially considered here. These equations were non-dimensionalized before obtaining a numerical approximation of the solution.

For some systems, the growth rate is controlled by the association rate of new monomer (i.e., reaction rate limited systems) while in other systems, the growth rate is controlled by the diffusion of gold atoms to the nanoparticle surface (i.e., diffusion limited systems) [27, 41]. If I is defined as the molar flux of gold to the surface of the nanoparticle and V_M is the molar volume, then the change in particle volume and radius is:

$$I = \frac{1}{V_M}\frac{dV}{dt} = \frac{4\pi r^2}{V_M}\frac{dr}{dt}. \qquad \text{Eq.15}$$

The total flux of molecules to the surface is proportional to particle radius (i.e., the characteristic diffusion length scale) for the diffusion limited case (i.e., $I = 4\pi r\mathcal{D}(C_b - C_{surface})$, and the total flux is proportional to particle surface area for the reaction limited case (i.e., $I = 4\pi r^2 k C_{surface}$). For the diffusion limited case, the rate at which particles are predicted to move from one size group, B_i, to the next group, B_{i+1}, is inversely related to the particle radius because $\frac{dr}{dt} = \frac{V_M}{r} \cdot \mathcal{D}(C_b - C_{surface})$. For the reaction rate limited case, $\frac{dr}{dt} = V_M k C_{surface}$. Experimental data from the system of interest here suggested that the growth rate of the nanoparticles was dependent on particle size (i.e., the system was diffusion limited) so the particle grow rate, $k_{2,i}$, was set to decrease as the particle radius increases:

$$k_{2,i} = \frac{k_2^o}{r_i} \qquad \text{Eq.16}$$

where k_2^o is an unknown growth rate constant. The population balance model predicts both the rate of nanoparticle formation but also the size distribution of the final population of nanoparticles.

The results of the model, the concentrations of particles of certain sizes, are converted to estimate of absorbance so that they can be compared with the experimental measurements taken using UV-vis spectrometry. Equations 5 and 7 were used to convert concentration to absorbance. For equation 7, particles in the same size group were assumed to have the same diameter and particles were assumed to grow in discrete amounts.

Numerical Implementation

Algorithms to numerically solve the system of ordinary differential equations associated with each model were developed and implemented using Python and the Scipy libraries. The initial value problems were solved using ODEPACK from Lawrence Livermore National Laboratory [42]. The initial conditions were set by assuming that no nanoparticles were present at the start of the simulation, and the initial concentration of insoluble gold atoms was set based on experimental measurements at various radiation doses. Finally, for both models, the unknown reaction rates (k_1, and k_2 for Finke-Wazky and k_1 and k_2^o for the population balance model) were determined by minimizing the L_2-

norm of the difference between experimental measurements and model prediction using either a Nelder-Mead simplex algorithm or manual parameter adjustment.

The Finke-Watzky Model

This simple model solves two differential equations, that describe nucleation and growth, for four hours (see algorithm in figure 5). The defined function "NucGrowth1", describes the set of differential equations that are derived from equations 5 and 6. The function requires an input of a vector 'C', that denotes the current particle concentrations for every size bin and a vector 't', that represents the current simulated time. The reaction coefficients are specified as parameters, so that they can be varied to search for the optimal values.

```
Tm=numpy.array([0,0.1,0.25,0.5,0.75,1,1.5,2,2.5,3,3.5,4])

def NucGrowth1(C,t,param):
    k1=param[0]
    k2=param[1]
    A=C[0];
    B=C[1];
    dAdt=-k1*A**n-k2*A*B
    dBdt=k1*A**n+k2*A*B
    return numpy.array([dAdt,dBdt])
```

Figure 5. "NucGrowth1" describes the set of differential equations that are derived from equations 5 and 6.

The results of the integration are particle concentrations for various sized particles, these are converted to absorbance by the function 'Absorbance.' The conversion is based on equations 5, 6 and 7, so that the concentrations can be compared

against the experimental data. As seen in figure 6, the “Absorbance” function requires a vector that contains concentration over time and particle diameters as inputs. The function ‘Error’ requires the experimental absorbance measurements and the simulated absorbance values at the same time points as inputs and calculates the difference between the model prediction and the experimental data. The function “runSim” executes the previously described functions and computes their outcome based on the two parameters, the reaction coefficients. The scipy.integrate library is used to solve the differential equations.

```
def Absorbance(S,D):
    E=math.exp(3.32111*math.log(D)+10.80505)
    atoms_per_particle=Na*AuM*(4/3*math.pi*((1e-8)*D/2)**3)
    C=(S[:,1])/atoms_per_particle #M
    A=C*E
    return A

def Error(S,Abs):
    error=0
    for i in range (numpy.size(Abs)):
        error += (S[i]-Abs[i])**2
    return numpy.sqrt(error)

def runSim(param):
    S=odeint(NucGrowth1,iC,Tm,args=(param,))
    A=Absorbance(S,D)
    error = Error(A,Abs)
    print error,param[0],param[1]
    return(error)
```

Figure 6. “Absorbance” converts gold concentration to the absorbance of gold nanoparticles. ‘Error’ compares the experimental Absorbance values with the model. “runSim” executes the previously described functions.

The difference between the model predictions and the data is calculated and minimized over several iterations of the code, while varying the two parameters, the reaction coefficients k_1 and k_2. Each time the code is run, the parameters are modified to determine new values that provide better agreement between the model prediction and the experimental data. After optimal parameter values are determined, they need to be inserted manually into the code. The scipy.optimize library was used to minimize the error.

```
error = runSim(kparams)
print error
minimize(runSim,kparams,bounds=((0,None),(0,None)))
```

Figure 7. The minimize command calculates the parameters that provide the closest results to the experimental data.

The Population Based Model

This model describes the growth of the particles using 50 successive ordinary differential equations, which represent balances on different particle size ranges. All the particles are assumed to have a radii between 0.5 nm (the smallest stable size) and 70 nm (the largest size observed experimentally in this system), and this radius range is separated into 50 size groups called bins. The differential equations describe the rates at which the particles change size groups. The minimum and maximum particle sizes were chosen based on experimental measurements. The constant parameter, ‘nucleus’ is set so that the smallest nuclei consist of 20 atoms. The function “atoms_bin” calculates the atoms required for a particle to transfer from one size group to the next, the only input necessary is the bin number.

```
bins = 50
max_radius = 6.91875e+1  #nm
min_radius = 5.0e-1 #nm
radius_bin = (max_radius-min_radius)/(bins-1)   #nm
nucleus=20
def atoms_bin(bin_num):
    V_bin=(4.0*math.pi/3.0)*(((min_radius+bin_num*radius_bin)**3)-
((min_radius+(bin_num-1)*radius_bin)**3)) #nm^3
    atom_bin=(V_bin*(1e-24))*(Na*AuM)
    return atom_bin
```

Figure 8. The experimentally determined range of possible particle radii is divided into 50 'bins', and the function "atoms_bin" calculates the size of each bin.

It was assumed that the growth rate constant, $k_{i,2}$, decreases as the particle size increases. The function "growth", calculates an individual growth rate constant for each size group. As seen in figure 9, the individual growth rates are based on an unknown constant and are inversely proportional to particle size and the gold atoms necessary for growing to the next size.

```
def growth(bin_num, params):
    k2=params[1]
    radius = min_radius+(bin_num-1)*radius_bin
    return k2 / ((radius)*atoms_bin(bin_num))
```

Figure 9. The function "growth" calculates an individual growth rate constant for each size group.

The function "df1" describes the system of differential equations to be solved and it requires the current particle concentration vector, 'N', the simulation time, 't', and the kinetic rate parameters, 'params', as inputs. As seen in figure 10, these equations are non-dimensionalized using the function "atoms_bin" and the constant defined as 'nucleus'. The function "Atotal" describes the equations that convert particle concentration to

absorbance based on particle size and sums the absorbance of all the particles for each timestep; it only requires a matrix of concentration at different time points as input.

```
def df1(N, t, params):
    n=4
    k1=params[0]
    dNdt = numpy.zeros(bins,dtype=numpy.float)
    dNdt[0] = -k1*N[0]**n - growth(1, params)*N[0]*N[1]
    dNdt[1] = k1*((N[0]**n)/nucleus) - growth(1,params)*N[0]*N[1]/atoms_bin(1)
    for i in range(2,bins-1):
        dNdt[0] = dNdt[0] - growth(i,params)* N[0]*N[i]
        dNdt[i] = growth(i-1, params)*N[0]*N[i-1]/atoms_bin(i-1) -
growth(i,params)*N[0]*N[i]/atoms_bin(i)
    dNdt[bins-1] = growth(bins-2,params)*N[0]*N[bins-2]/atoms_bin(bins-2)
    return numpy.array(dNdt)

def Atotal(C):
    (m,n)=numpy.shape(C)
    Atot=numpy.zeros(m)
    for i in range (0,m):
        for j in range (0,n):
            if C[i,j]<0:
                C[i,j]=0
            radius = min_radius+(j)*radius_bin
            Atot[i]+=1*(C[i,j]*1e-6)*math.exp(k*math.log1p(radius*2)+a
    return numpy.array(Atot)
```

Figure 10. The function that describes the system of differential equations to be solved, “df1” and the function that converts particle concentrations over time to absorbance over time, “Atotal”.

The current simulation code runs the simulation 6 times, once for each unique radiation dose, and calculates the particle size distributions which are compared with the experimental distributions. The minimize function could not be used in conjunction with this code due to the high computational cost for a single set of parameters. Instead,

optimal parameter values were determined by manually testing various parameter values to obtain the best possible agreement with the experimental data.

Computational Cost

The process time of the simulation was recorded using the "time.process_counter()" command. For this measurement, an Alienware laptop with Intel Core© i7-6820HK CPU @2.70GHz processor and 8.00 GB RAM was used. Figure 11 shows the processing time increase as the number of bins increases. The empirical data suggests that the process time has the following relation to the number of unique particle size bins:

$$t = 0.0068n^2 + 0.3969n - 0.699 \qquad \text{Eq.16}$$

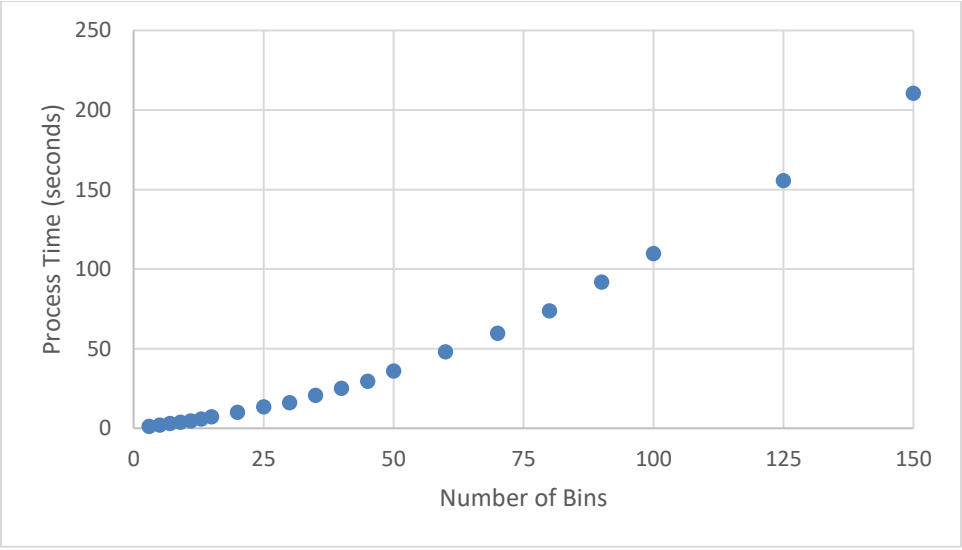

Figure 11. Process time (seconds) versus number of bins.

CHAPTER THREE: RESULTS AND DISCUSSION

The Finke-Watzky Model

The Finke-Watzky model prediction for the conversion of gold atoms into gold nanoparticles using optimal values for the reaction rates so that the model predictions match the experimental data are shown below in Figure 12. The experimental data shown in Figure 12 is from experimental measurements of absorbance after exposure to a radiation dose of 15 Gy. The initial gold salt concentration is 0.0109 mM and size measurements show that the mean particle diameter is 88.46 nm. Under these conditions, the optimal values for the kinetic parameters, k_1, and k_2, are 1 min^{-1} and $3 * 10^5$ $min^{-1}M^{-1}$, respectively.

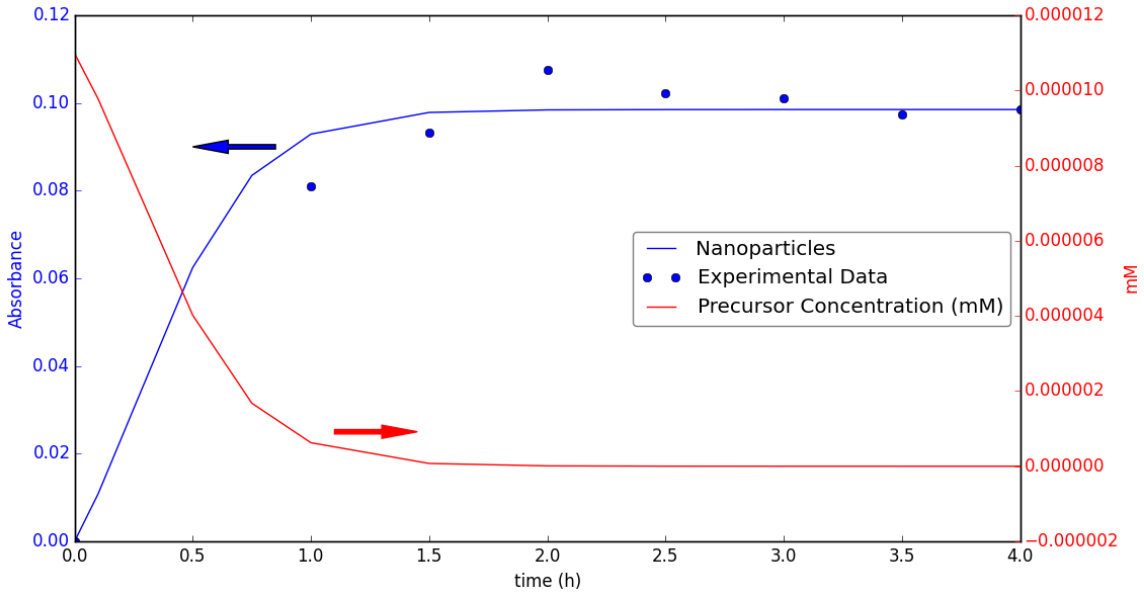

Figure 12. The Finke -Watzky model prediction for the precursor concentration and the absorbance of gold- nanoparticles over time for 15 Gy radiation dosage.

Figure 13, shows how the same kinetic parameters that provided the best fit for the median dosage, 15 Gy, fit the model to experimental data at other radiation dosages. Unfortunately, this model does not predict the size distribution of the nanoparticles so comparisons with nanoparticle size measurements are not possible. The model predictions are least accurate for the 5 Gy case where GNP formation is predicted to occur more rapidly that is observed experimentally. Overall, however, the model agreement with the experimental data is good.

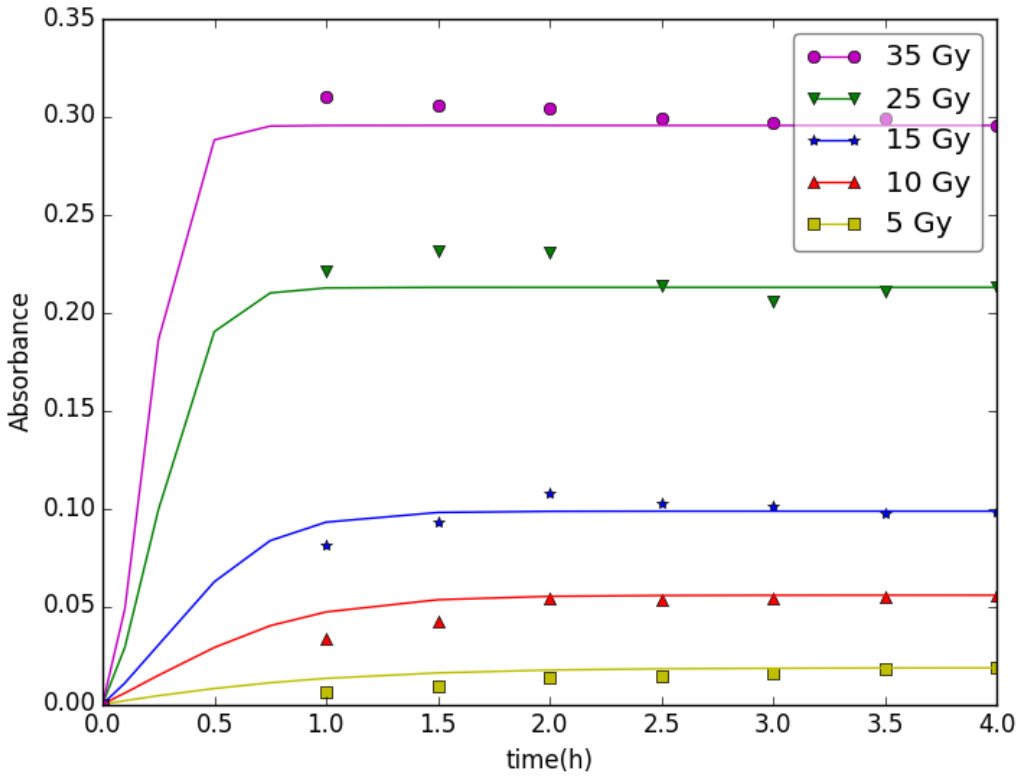

Figure 13. The absorbance predictions for various radiation doses.

The Population Balance Model

The next set of results are based on the population balance model. Figure 14 shows the model prediction of absorbance versus time for a range of different radiation doses from 5 to 35 Gy. The kinetic parameters, k_1, and k_2, are $8 * 10^{-10}$ min^{-1} and $3 * 10^{13}$ $m^4 min^{-1} \mu M^{-1}$, respectively, and n is set to 4. Unfortunately, the earliest experimental measurements of absorbance are 60 minutes after the radiation dose was delivered so the initial rate of change in absorbance cannot be compared between the model and the experimental data.

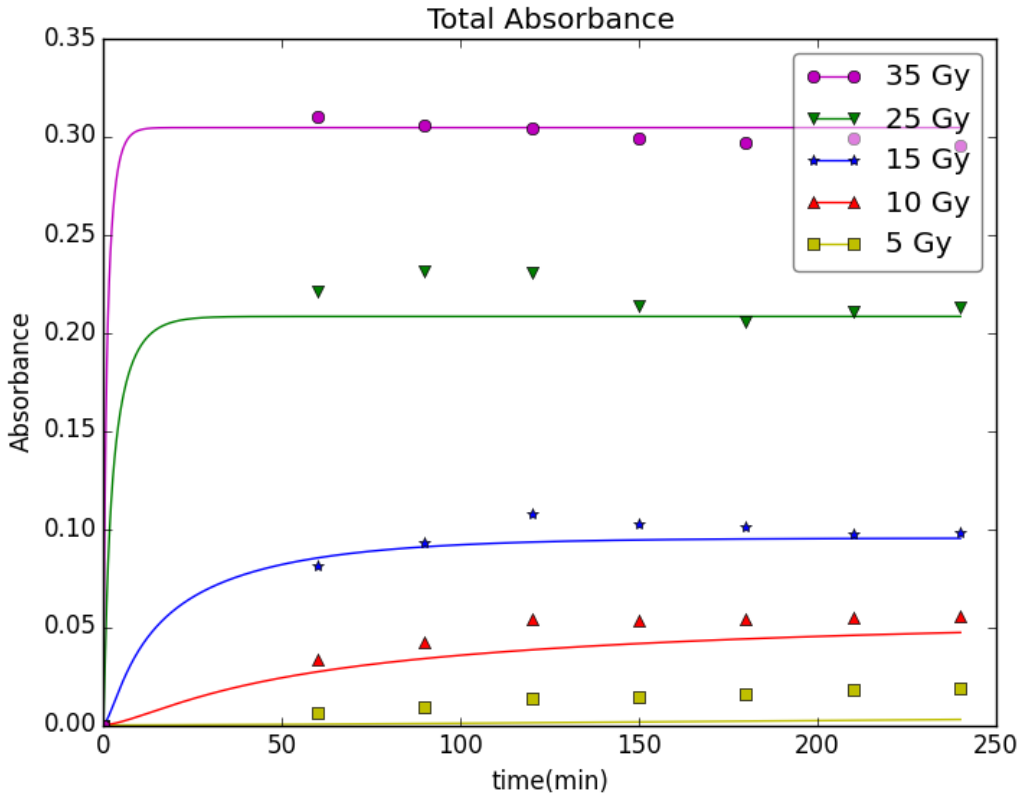

Figure 14. Absorbance versus time(min) for different radiation doses (Gy).

The agreement between the model predictions and the experimental measurements is the strongest at radiation doses of 15 Gy or higher, and the agreement is weakest at the 5 Gy dose. This discrepancy is probably due to the slower than actual nucleation rate used in the model, but could also be due to error in the measurement of the initial, reduced gold atom concentration, i.e., the initial concentration of Au^0. The initial concentration is determined by first measuring the gold salt concentration (i.e., the Au^{3+} concentration) and then measuring soluble gold concentration after radiation exposure (i.e., measuring the Au^{3+} that was not converted to Au^0 by radiation exposure). At the lower radiation doses (5 and 10 Gy), less of the gold salt was converted to Au^0 and this smaller quantity could be more difficult to accurately determine. Hence, the experimental error in measuring the initial Au^0 concentration is most likely greatest for the lowest radiation doses, and this error could help explain the differences between the experimental measurements and model predictions seen in Figure 14.

Figure 15 shows the model prediction for the final particle size distribution for different radiation doses using the same model parameters as Figure 14. The vertical, dashed lines represent the experimental measurements of median particle size for the various radiation doses. The model predictions agree with the experimental observation that the mean particle size decreases as the radiation dose is increased. For higher radiation doses, there is a higher initial concentration of Au^0 atoms and the formation of the smallest stable nanoparticles (i.e., nucleation) is more rapid. The numerous small nanoparticles quickly grow, but all the Au^0 in the solution is consumed before the particles are very large (i.e., when they are still only 35-40 nm). Conversely, at lower radiation doses, the smaller

Au^0 concentration results in less nucleation and fewer nanoparticles, overall. Even though the Au^0 concentration is lower, the small number of nanoparticles allows the particles to grow much larger before the Au^0 concentration drops to very low levels.

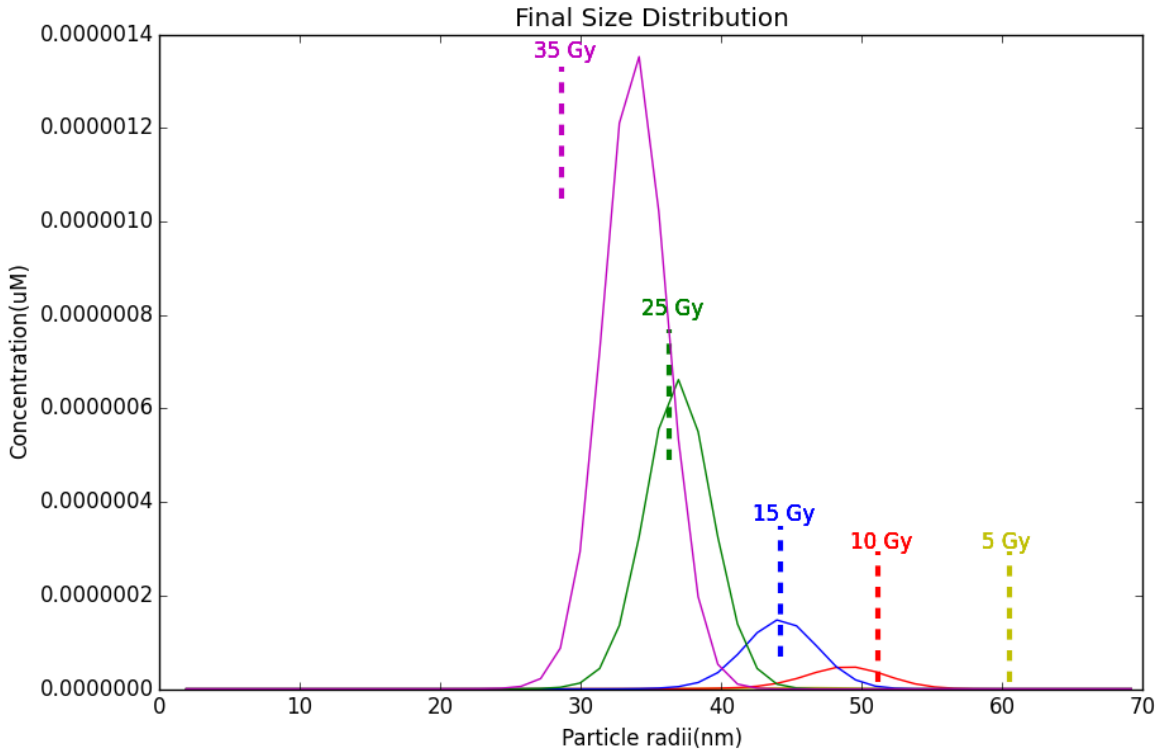

Figure 15. The particle concentration versus simulated particle radius at varying radiation doses (Gy). Higher radiation doses result in more abundant but smaller particles.

The agreement between the model and the experimental measurements is best at the middle radiation doses (15 and 25 Gy), but in the largest radiation doses, the model prediction is for larger particles than what was measured experimentally. One possible explanation for this is that the model includes a maximum particle size that cannot be exceeded. If a few experimental particles exceed this maximum particle size (an event that almost certainly occurred), then less Au^0 was available for particle growth in the

experiment than in the corresponding model prediction. As a result, most of the experimental particles would be slightly smaller than predicted by the model because a few particles are much larger than predicted by the model.

Another possible explanation for the larger particles predicted by the model is that the model assumed diffusion was limiting the particle growth rate so that the rate constant, $k_{i,2}$, was inversely related to the particle radius. This is only a 1-dimensional approximation of the diffusion limitation effects, and a full diffusion model for each particle could reveal an even greater change in the rate constant as the particle radius increases, thus leading to greater slowing of the growth of particles at high concentrations (i.e., high Gy) and reducing the mean particle size predicted by the model.

One more explanation for the smaller particles observed experimentally is that the nucleation rate is faster than modeled, especially for the highest radiation doses. The nucleation rate is proportional to A^4, or the reduced gold atom concentration $[Au^0]^4$. This implies that a doubling of the initial Au^0 concentration results in a nucleation rate that is 16-times faster. Using a non-integer exponent (e.g., 4.5) could result in slightly faster nucleation and the more abundant particle number would limit particle size providing better agreement between the model the experimental data.

Model Parameter Sensitivity Analysis

Figure 16 shows how the results of the PBM model are affected by changes in the nucleation rate, k_1. Halving the nucleation rate to 4×10^{-10} min^{-1}, decreases the initial slope of the absorbance predictions while increasing the particle sizes. As expected, slower nucleation leads to fewer initial nuclei to be formed, leaving behind more precursor to be used for growth. This results in a slower increase in Absorbance and decreased particle concentrations for all radiation doses. The leftover precursor allows the particles to grow bigger, creating fewer but larger particles. Doubling the nucleation rate to 1.6×10^{-9} min^{-1}, has the opposite effects. Faster nucleation leads to more nuclei, which results in a faster increase in Absorbance and increased particle concentrations for all radiation doses. The production of extra nuclei consumes precursor and limits the growth of the particles, creating more but smaller particles.

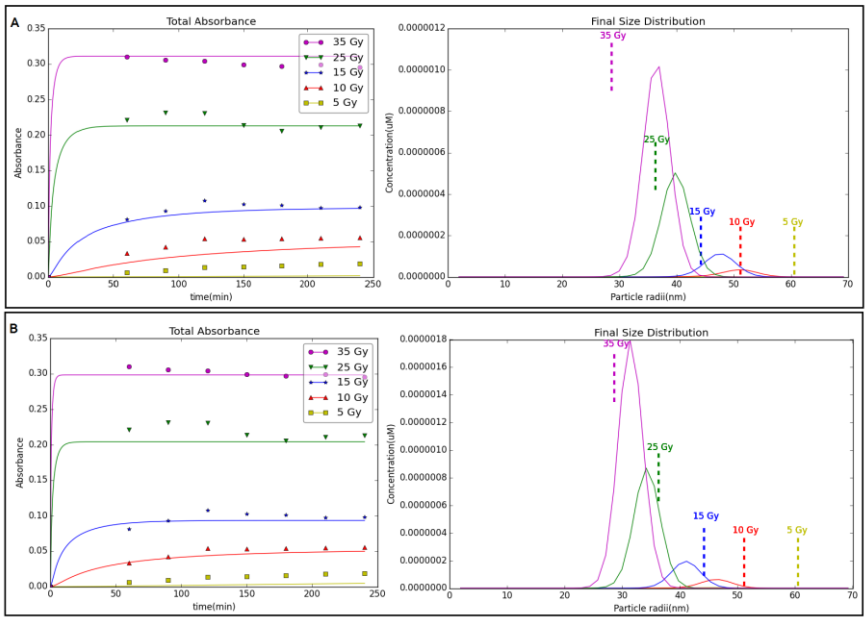

Figure 16. The absorbance and particle distribution predictions of the PBM model with A) half the nucleation rate and B) double the nucleation rate.

Figure 17 shows how the results of the PBM model are affected by changes in the growth rate, k_2. Halving the growth rate to 1.5×10^{13} $m^4min^{-1}\mu M^{-1}$, decreases the initial slope of the absorbance predictions while also decreasing the particle sizes. As expected, slower growth allows more initial nuclei to form, leaving less precursor for growth. This results in a slightly slower increase in Absorbance and increased particle concentrations for all radiation doses. The production of extra nuclei consumes precursor and limits the growth of the particles, creating more, smaller particles. Doubling the growth rate to 6×10^{13} $m^4min^{-1}\mu M^{-1}$, has the opposite effects. Faster growth leads to fewer nuclei having a chance to form before all the precursor is consumed. The result is a more rapid increase in Absorbance, decreased particle concentrations, and larger particles for all radiation doses.

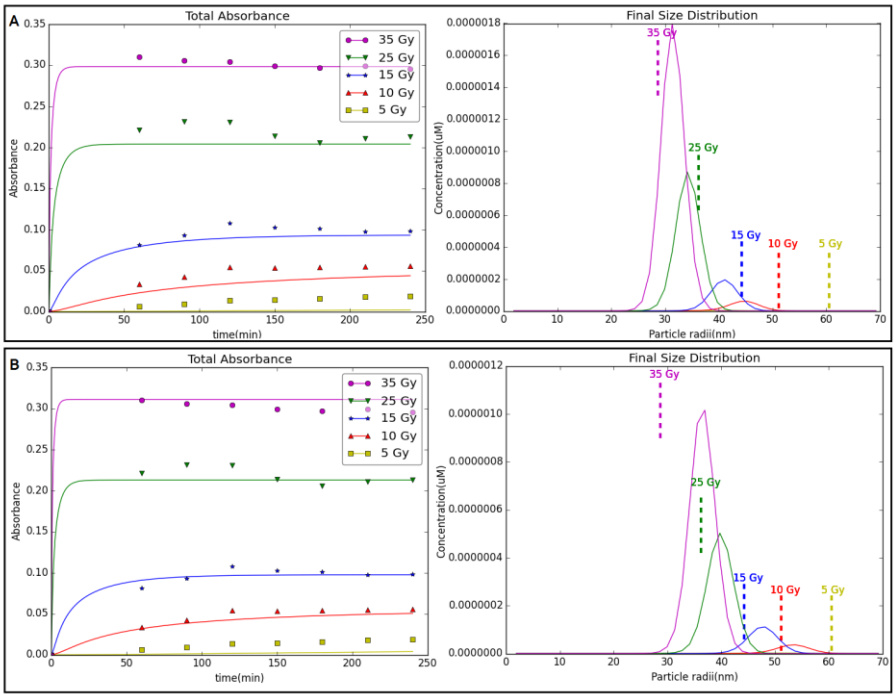

Figure 17. The absorbance and particle distribution predictions of the PBM model with A) half the growth rate and B) double the growth rate.

The particle distributions are a result of the nucleation and growth reactions competing for precursor. The exponent on the precursor concentration in the nucleation reaction, n, increases the rate at which nucleation occurs, and more rapid nucleation generates more competition with the growth reaction for the limited supply of precursor. Figure 17, shows the effect of changing the precursor consumption power on the GNP size distribution.

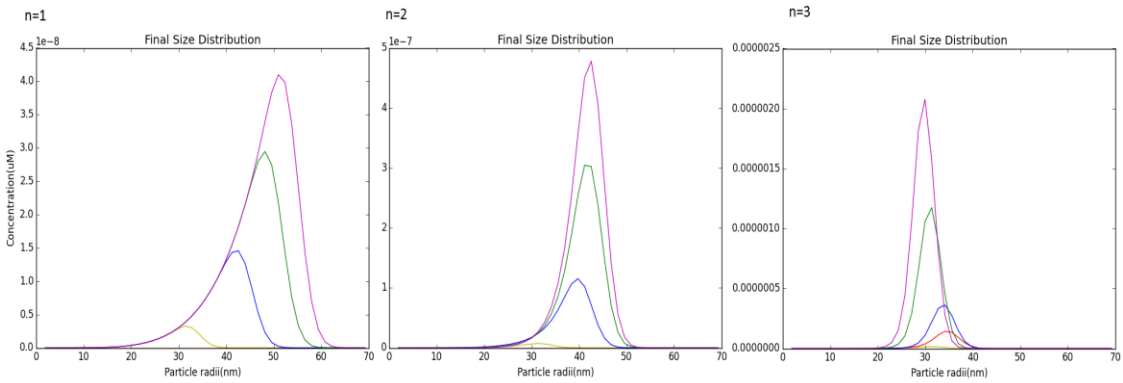

Figure 18. The particle distribution as the precursor consumption power, n, is increased.

For the case of slower nucleation, $n = 1$, higher radiation doses always result in larger particles because higher radiation doses create more precursor and the additional precursor results in larger GNPs. This result directly contradicts what is observed experimentally. For the $n = 2$ and $n = 3$ cases, nucleation is more rapid, especially at the higher radiation doses, so we start to see the highest doses generating smaller particles because of precursor depletion, but the particle sizes at different radiation doses are still less variable than what was observed experimentally. The optimal agreement with the experimental measurements is $n = 4$, as shown in Figure 15.

CHAPTER FOUR: CONCLUSIONS

Mathematical models of gold nanoparticle formation kinetics following radiation exposure were developed and compared to experimental measurements of absorbance and particle size. The first mathematical model was based on the Finke-Watzke model. The model is relatively simple to implement and parameter optimization using experimental data is straightforward. Unfortunately, model agreement with the experimental system of interest here was only optimal for one radiation dose, and the model parameters needed to be changed for other radiation doses to retain a high quality fit with the data. The greatest limitation of the Finke-Watzke model is that it only predicts the precursor consumption rate and it does not predict the final particle size distribution.

The second mathematical model developed here was based on a population balance model. This model is more difficult to implement and has greater computational requirements. The model prediction of absorbance at different radiation doses was good for the lower doses, but there was less agreement at the highest doses. The particle size distribution prediction was consistent and often very close to the experimental measurements. For all radiation doses, the model predicted a larger mean particle size than was observed experimentally, and some possible explanations for this discrepancy were given the results and discussion section.

Future Work

The mathematical model of GNP formation following radiation exposure presented in this thesis can be improved in a number of ways. First, secondary nucleation effects can potentially be taken into account by modelling effects like Ostwald ripening and coalescence of nuclei could improve the fit of the initial nucleation. Additional data on GNP formation could also be used to improve the fit of the model. In particular, absorbance data during the first few minutes would be extremely valuable. Halting the reactions at various time points to provide particle size data at intermediate time points would also be valuable.

The original motivation for the development of the model presented here was to improve the radiation dose measurement abilities of the GNP system at low radiation doses. So to close this thesis, what can the current model tell us about increasing absorbance at low radiation doses? Comparing 10 Gy to 25 Gy, we can observe that the GNPs resulting from a 25 Gy dose absorbed 4 times the amount of light relative to 10 Gy, but the number of particles at 25 Gy was 6 times the number at 10 Gy. Clearly, fewer, larger particles at 10 Gy provide a greater color change relative to the number of particles than at 25 Gy. Any change that slows down nucleation slightly so that particles can grow larger has the potential to improve system performance. Exploring alternative templating molecules and adjusting gold salt concentrations both have the potential to improve system performance at low radiation doses. Seeding the solution with stable nuclei so that more of the gold is captured in particle growth also has the potential to improve low dose performance.

REFERENCES CITED

1 Anderson, M.L., et al., *Colloidal gold aerogels: Preparation, properties, and characterization.* Langmuir, 1999. **15**(3): p. 674-681.

2 Freestone, I., et al., *The Lycurgus Cup - A Roman nanotechnology.* Gold Bulletin, 2007. **40**(4): p. 270-277.

3 Faraday, M., *The Bakerian Lecture: Experimental Relations of Gold (and Other Metals) to Light.* Philosophical Transactions of the Royal Society of London, 1857. **147**: p. 145-181.

4 Fetni, R., et al., *Simultaneous Visualization of Chromosome Bands and Hybridization Signal Using Colloidal-Gold Labeling in Electron-Microscopy.* Proceedings of the National Academy of Sciences of the United States of America, 1991. **88**(23): p. 10916-10920.

5 Pankhurst, Q.A., et al., *Progress in applications of magnetic nanoparticles in biomedicine.* Journal of Physics D-Applied Physics, 2009. **42**(22).

6 Huang, D., et al., *Plastic-compatible low resistance printable gold nanoparticle conductors for flexible electronics.* Journal of the Electrochemical Society, 2003. **150**(7): p. G412-G417.

7 Narayanan, R. and M.A. El-Sayed, *Catalysis with transition metal nanoparticles in colloidal solution: Nanoparticle shape dependence and stability.* Journal of Physical Chemistry B, 2005. **109**(26): p. 12663-12676.

8 Bonnemann, H. and R.M. Richards, *Nanoscopic metal particles - Synthetic methods and potential applications.* European Journal of Inorganic Chemistry, 2001(10): p. 2455-2480.

9 Hyeon, T., *Chemical synthesis of magnetic nanoparticles.* Chemical Communications, 2003(8): p. 927-934.

10 Sozer, N. and J.L. Kokini, *Nanotechnology and its applications in the food sector.* Trends in Biotechnology, 2009. **27**(2): p. 82-89.

11 Atwater, H.A. and A. Polman, *Plasmonics for improved photovoltaic devices (vol 9, pg 205, 2010).* Nature Materials, 2010. **9**(10): p. 865-865.

12 Turkevich, J., P.C. Stevenson, and J. Hillier, *A Study of the Nucleation and Growth Processes in the Synthesis of Colloidal Gold.* Discussions of the Faraday Society, 1951(11): p. 55-&.

13 Kimling, J., et al., *Turkevich method for gold nanoparticle synthesis revisited.* Journal of Physical Chemistry B, 2006. **110**(32): p. 15700-15707.

14 Frens, G., *Controlled Nucleation for Regulation of Particle-Size in Monodisperse Gold Suspensions.* Nature-Physical Science, 1973. **241**(105): p. 20-22.

15 Perrault, S.D. and W.C.W. Chan, *Synthesis and Surface Modification of Highly Monodispersed, Spherical Gold Nanoparticles of 50-200 nm.* Journal of the American Chemical Society, 2009. **131**(47): p. 17042-+.

16 Martin, M.N., et al., *Charged Gold Nanoparticles in Non-Polar Solvents: 10-min Synthesis and 2D Self-Assembly.* Langmuir, 2010. **26**(10): p. 7410-7417.

17 Hanzic, N., et al., *The synthesis of gold nanoparticles by a citrate-radiolytical method.* Radiation Physics and Chemistry, 2015. **106**: p. 77-82.

18 Thomas, S., et al., *Complexation of gold and silver nanoparticles with radiolytically-generated radicals.* Research on Chemical Intermediates, 2005. **31**(7-8): p. 595-603.

19 Seth, R.K., et al., *Ionizing radiation as a phytosanitary treatment against Phenacoccus solenopsis (Hemiptera: Pseudococcidae).* Florida Entomologist, 2016. **99**(Sup): p. 76-87.

20 Boal, T., P.A. Colgan, and R. Czarwinski, *International Basic Safety Standards - Protecting people and the environment.* Radioprotection (EDP Sciences), 2013. **48**(S1): p. S27-S33.

21 Hill, R., et al., *Advances in kilovoltage x-ray beam dosimetry.* Physics in Medicine and Biology, 2014. **59**(6): p. R183-R231.

22 Pardue, L.A., N. Goldstein, and E.O. Wollan, *Photographic film as a pocket radiation dosimeter.* At Energy Biophys Biol Med, 1948. **1**(5): p. 169.

23 Zhang, Z., C. Kleinstreuer, and C.S. Kim, *Micro-particle transport and deposition in a human oral airway model.* Journal of Aerosol Science, 2002. **33**(12): p. 1635-1652.

24 Fiandra, C., et al., *Comparison of Gafchromic EBT2 and EBT3 for patient-specific quality assurance: Cranial stereotactic radiosurgery using volumetric modulated arc therapy with multiple noncoplanar arcs.* Medical Physics, 2013. **40**(8).

25 Lamer, V.K. and R.H. Dinegar, *Theory, Production and Mechanism of Formation of Monodispersed Hydrosols.* Journal of the American Chemical Society, 1950. **72**(11): p. 4847-4854.

26 Lamer, V.K., *Nucleation in Phase Transitions.* Industrial and Engineering Chemistry, 1952. **44**(6): p. 1270-1277.

27 Thanh, N.T.K., N. Maclean, and S. Mahiddine, *Mechanisms of Nucleation and Growth of Nanoparticles in Solution.* Chemical Reviews, 2014. **114**(15): p. 7610-7630.

28 Wagner, C., *Theorie Der Alterung Von Niederschlagen Durch Umlosen (Ostwald-Reifung).* Zeitschrift Fur Elektrochemie, 1961. **65**(7-8): p. 581-591.

29 Lifshitz, I.M. and V.V. Slyozov, *The Kinetics of Precipitation from Supersaturated Solid Solutions.* Journal of Physics and Chemistry of Solids, 1961. **19**(1-2): p. 35-50.

30 Lee, W.R., et al., *Redox-transmetalation process as a generalized synthetic strategy for core-shell magnetic nanoparticles.* J Am Chem Soc, 2005. **127**(46): p. 16090-7.

31 Watzky, M.A. and R.G. Finke, *Nanocluster size-control and "magic number" investigations, experimental tests of the "living-metal polymer" concept and of mechanism-based size-control predictions leading to the syntheses of iridium(0) nanoclusters centering about four sequential magic numbers.* Chemistry of Materials, 1997. **9**(12): p. 3083-3095.

32 Georgiev, P., et al., *Implementing atomic force microscopy (AFM) for studying kinetics of gold nanoparticle's growth.* Colloids and Surfaces a-Physicochemical and Engineering Aspects, 2013. **434**: p. 154-163.

33 Watzky, M.A., E.E. Finney, and R.G. Finke, *Transition-metal nanocluster size vs formation time and the catalytically effective nucleus number: A mechanism-based treatment.* Journal of the American Chemical Society, 2008. **130**(36): p. 11959-11969.

34 Besson, C., E.E. Finney, and R.G. Finke, *A mechanism for transition-metal nanoparticle self-assembly.* Journal of the American Chemical Society, 2005. **127**(22): p. 8179-8184.

35 Yao, S.Y., et al., *Insights into the Formation Mechanism of Rhodium Nanocubes.* Journal of Physical Chemistry C, 2012. **116**(28): p. 15076-15086.

36 Perala, S.R.K. and S. Kumar, *On the Two-Step Mechanism for Synthesis of Transition-Metal Nanoparticles.* Langmuir, 2014. **30**(42): p. 12703-12711.

37 Turnbull, D. and J.C. Fisher, *Rate of Nucleation in Condensed Systems.* Journal of Chemical Physics, 1949. **17**(1): p. 71-73.

38 Thomas, N. and E. Mani, *An analytical solution to the kinetics of growth of gold nanorods.* Rsc Advances, 2016. **6**(36): p. 30028-30036.

39 Liu, X.O., et al., *Extinction coefficient of gold nanoparticles with different sizes and different capping ligands.* Colloids and Surfaces B-Biointerfaces, 2007. **58**(1): p. 3-7.

40 Yu, F., *From molecular clusters to nanoparticles: second-generation ion-mediated nucleation model.* Atmospheric Chemistry and Physics, 2006. **6**: p. 5193-5211.

41 Rempel, J.Y., M.G. Bawendi, and K.F. Jensen, *Insights into the Kinetics of Semiconductor Nanocrystal Nucleation and Growth.* Journal of the American Chemical Society, 2009. **131**(12): p. 4479-4489.

42 Byrne, G.D. and A.C. Hindmarsh, *PVODE, an ODE solver for parallel computers.* International Journal of High Performance Computing Applications, 1999. **13**(4): p. 354-365.

APPENDICES

APPENDIX A

THE FINKE-WATZKY CODE (FW.py)

```
import pylab
import numpy
import math
import matplotlib.pyplot as plt
from scipy.integrate import odeint
from scipy.optimize import minimize
import matplotlib.lines as mlines

kparams=[1, 3*10**5] #while n=1, k1=2,k2=10000
n=1
Na = 6.02214e+23 # Avogadro's constant in 1/mol
AuM = 98.0 # molar density in mol/L

#Data
Grays=numpy.array([0.0,5.0,10.0,15.0,25.0,35.0])
AvgDiameters=numpy.array([0.0,1.21105e-7, 1.02325e-7, 8.8465e-8, 7.25875e-8,5.727e-8])#m
Absorbances=numpy.matrix([[0.0,0.002333333,0.002666667,0.003733333,0.001633333,0.00173
3333,0.0025,0.001733333],[0.0,0.0062,0.0093,0.013433,0.0144,0.015567,0.018167,0.018633],[0
.0,0.033366667,0.042,0.054066667,0.053266667,0.053933333,0.054866667,0.055633333],[0.0,0
.0809,0.0931333333,0.1076333333,0.1022666667,0.1009666667,0.0973333333,0.0985],[0.0,0.2
208,0.231,0.230733333,0.213866667,0.205266667,0.210433333,0.2127],[0.0,0.31,0.305633333,
0.3042,0.299133333,0.2968,0.2987,0.2953]])

num=3 #0=0,1=5,2=10,3=15,4=25,5=35
D=(1e+9)*AvgDiameters[num] #nm
Abs=numpy.squeeze(numpy.asarray(Absorbances[num,:]))
iC=numpy.array([Absorbances[num,-
1]/math.exp(3.32111*math.log(D)+10.80505)*Na*AuM*(4/3*math.pi*((1e-
8)*D/2)**3),0.0])#M

Td=numpy.array([0,1,1.5,2,2.5,3,3.5,4])
Tm=numpy.array([0,0.1,0.25,0.5,0.75,1,1.5,2,2.5,3,3.5,4])

def NucGrowth1(C,t,param):
    k1=param[0]
    k2=param[1]
    A=C[0];
    B=C[1];
    dAdt=-k1*A**n-k2*A*B
    dBdt=k1*A**n+k2*A*B
    return numpy.array([dAdt,dBdt])

def Absorbance(S,D):
    E=math.exp(3.32111*math.log(D)+10.80505)
    atoms_per_particle=Na*AuM*(4/3*math.pi*((1e-8)*D/2)**3)
    C=(S[:,1])/atoms_per_particle #M
```

```
    A=C*E
    return A

def Error(S,Abs):
    error=0
    for i in range (numpy.size(Abs)):
        error += (S[i]-Abs[i])**2
    return numpy.sqrt(error)

def runSim(param):
    S=odeint(NucGrowth1,iC,Tm,args=(param,))
    A=Absorbance(S,D)
    error = Error(A,Abs)
    print error,param[0],param[1]
    return(error)

def showplots(param):
    S=odeint(NucGrowth1,iC,Tm,args=(param,))
    A=Absorbance(S,D)
    fig,ax1=plt.subplots()
    ax1.plot(Tm, A[:], 'b-')
    ax1.plot(Td,Abs,'bo')
    ax1.set_xlabel('time (h)')
    ax1.set_ylabel('Absorbance', color='b')
    ax1.tick_params('y', colors='b')
    pylab.arrow(0.85, 0.09, -0.2, 0, head_width=0.003, head_length=0.15)
    pylab.arrow(1.1, 0.025, 0.2, 0, head_width=0.003, head_length=0.15,color='r')
    ax2 = ax1.twinx()
    ax2.plot(Tm, S[:,0], 'rs-')
    ax2.set_ylabel('mM', color='r')
    ax2.tick_params('y', colors='r')
    l1=mlines.Line2D([],[],color='b',label='Nanoparticles')
    l2=mlines.Line2D([],[],color='b',linewidth='0', marker='o',label='Experimental Data')
    l3=mlines.Line2D([],[],color='r',marker='s',label='Precursor Concentration (mM)')
    plt.legend(handles=[l1,l2,l3],fancybox=True, framealpha=0.5,loc='center right')
showplots(kparams)

error = runSim(kparams)
print error
minimize(runSim,kparams,bounds=((0,None),(0,None)))

pylab.figure(2)
y=mlines.Line2D([],[],marker='s',color='y',label='5 Gy')
r=mlines.Line2D([],[],marker='^',color='r',label='10 Gy')
b=mlines.Line2D([],[],marker='*',color='b',label='15 Gy')
g=mlines.Line2D([],[],marker='v',color='g',label='25 Gy')
m=mlines.Line2D([],[],marker='o',color='m',label='35 Gy')
plt.legend(handles=[m,g,b,r,y],fancybox=True, framealpha=0.5,loc=1)
plt.xlabel('time(h)')
```

```
plt.ylabel('Absorbance')
colors=numpy.array(['c','y','r','b','g','m'])
ocolors=numpy.array(['ch','ys','r^','b*','gv','mo'])

for N in range (1,6): #0=0,1=5,2=10,3=15,4=25,5=35
   D=(1e+9)*AvgDiameters[N] #nm
   Abs=numpy.squeeze(numpy.asarray(Absorbances[N,:]))
   ic=Absorbances[N,-
1]/math.exp(3.32111*math.log(D)+10.80505)*Na*AuM*(4/3*math.pi*((1e-8)*D/2)**3) #M
   iC=numpy.array([ic,0.0])
   S=odeint(NucGrowth1,iC,Tm,args=(kparams,))
   A=Absorbance(S,D)
   pylab.plot(Td,Abs,ocolors[N],Tm,A,colors[N])
   print ic, A[-1]
```

APPENDIX B

THE POPULATION BALANCE MODEL CODE (PBM.py)

```
import numpy
import pylab
import math
import matplotlib.lines as mlines
import matplotlib.pyplot as plt
from scipy.integrate import odeint

Na = 6.02214e+23 # Avogadro's constant in 1/mol
AuM = 98.0 # molar density in mol/L
k=3.32111;a=10.80505                #absorbance coefficients

#Data
TIME=numpy.asarray([0.0,1.0,1.5,2.0,2.5,3.0,3.5,4.0])#h
Grays=numpy.array([0.0,5.0,10.0,15.0,25.0,35.0])
AvgDiameters=numpy.array([0.0,1.21105e-7, 1.02325e-7, 8.8465e-8, 7.25875e-8,5.727e-8])#m
AvgBins=numpy.array([0.0,33,20,13,7,4])#for 50 bins total
Absorbances=numpy.matrix([[0.0,0.002333333,0.002666667,0.003733333,0.001633333,0.00173
3333,0.0025,0.001733333],[0.0,0.0062,0.0093,0.013433,0.0144,0.015567,0.018167,0.018633],[0
.0,0.033366667,0.042,0.054066667,0.053266667,0.053933333,0.054866667,0.055633333],[0.0,0
.0809,0.0931333333,0.1076333333,0.1022666667,0.1009666667,0.0973333333,0.0985],[0.0,0.2
208,0.231,0.230733333,0.213866667,0.205266667,0.210433333,0.2127],[0.0,0.31,0.305633333,
0.3042,0.299133333,0.2968,0.2987,0.2953]])
ICs=numpy.array([0.003257421,0.039755701,0.036040704,0.018990198,0.075461916,0.069681
971])#mM
ICarb=numpy.array([0.0003,0.0018,0.0075,0.013,0.03,0.04])#mM
colors=numpy.array(['c','y','r','b','g','m'])
ocolors=numpy.array(['ch','ys','r^','b*','gv','mo'])

bins = 50
max_radius = 6.91875e+1  #nm
min_radius = 5.0e-1 #nm
radius_bin = (max_radius-min_radius)/(bins-1)   #radius increase per bin #nm
nucleus=20        #atoms required for nucleation(mol atoms/mol particles)

#Functions
def atoms_bin(bin_num):
    V_bin=(4.0*math.pi/3.0)*(((min_radius+bin_num*radius_bin)**3)-((min_radius+(bin_num-
1)*radius_bin)**3)) #nm^3
    atom_bin=(V_bin*(1e-24))*(Na*AuM)
    return atom_bin

def growth(bin_num, params): #individual growth coeff(k2) for each size
    k2=params[1]
    radius = min_radius+(bin_num-1)*radius_bin # radius in nm
    return k2 / ((radius)*atoms_bin(bin_num))
```

```
def df1(N, t, params):                    # ODE definition
   n=4
   k1=params[0]
   dNdt = numpy.zeros(bins,dtype=numpy.float)
   dNdt[0] = -k1*N[0]**n - growth(1, params)*N[0]*N[1]
   dNdt[1] = k1*((N[0]**n)/nucleus) - growth(1,params)*N[0]*N[1]/atoms_bin(1)
   for i in range(2,bins-1):
      dNdt[0] = dNdt[0] - growth(i,params)* N[0]*N[i]
      dNdt[i] = growth(i-1, params)*N[0]*N[i-1]/atoms_bin(i-1) -
growth(i,params)*N[0]*N[i]/atoms_bin(i)
   dNdt[bins-1] = growth(bins-2,params)*N[0]*N[bins-2]/atoms_bin(bins-2)
   return numpy.array(dNdt)

def Atotal(C):                            #Absorbance conversion
   (m,n)=numpy.shape(C)
   Atot=numpy.zeros(m)
   for i in range (0,m):
      for j in range (0,n):
         if C[i,j]<0:
            C[i,j]=0
         radius = min_radius+(j)*radius_bin #nm
         Atot[i]+=1*(C[i,j]*1e-6)*math.exp(k*math.log1p(radius*2)+a)# diameter must be in nm,
conc must be M
   return numpy.array(Atot)

def MassBalance(C):
   (m,n)=numpy.shape(C)
   mass=numpy.zeros(m)
   partmass=numpy.zeros(m)
   Prec=C[:,0]
   for i in range (0,m):
      for j in range (1,n):
         if C[i,j]<0:
            C[i,j]=0
         radius = min_radius+(j)*radius_bin #nm
         partmass[i]+=C[i,j]*Na*AuM*(4/3*math.pi*((1e-8)*radius)**3) #uM
         mass[i]=partmass[i]+Prec[i]
   return numpy.array([Prec,partmass,mass])

Radius=numpy.zeros(bins-1)
for i in range (0,bins-1):
   Radius[i] =(min_radius+(i+1)*radius_bin) #nm

for num in range (1,6): #0=0,1=5,2=10,3=15,4=25,5=35
   N0= numpy.zeros(bins,dtype=numpy.float)
   Abs=numpy.ndarray.flatten(numpy.asarray(Absorbances[num]))
   D=(1e+9)*AvgDiameters[num] #nm
```

```
   N0[0]=1.25*(Absorbances[num,-
1]/math.exp(3.32111*math.log(D)+10.80505)*Na*AuM*(4/3*math.pi*((1e-8)*D/2)**3))*1e+6
#uM

#Checkpointing
   endtime=4*60       #min
   tsteps = 2000*numpy.size(Abs)              #timesteps #should be 5000
   T= numpy.linspace(0.0,endtime,tsteps)      #Initial Time span

   kparams1=numpy.array([8e-11, 3*3e+12])     #k1,k2(1/min,m^4/uMmin)
   S1 = odeint(df1, N0, T, args=(kparams1,),rtol=1e-9,atol=1e-9,hmax=1e-1,mxstep=5000) #uM
   Prec=S1[:,0]   #uM
   M=MassBalance(S1)#uM
   S1=numpy.delete(S1,(0),axis=1)

   Atot=Atotal(S1)              #Concentration to absorbance conversion

#Plotting
   pylab.figure(1)
   y=mlines.Line2D([],[],marker='s',color='y',label='5 Gy')
   r=mlines.Line2D([],[],marker='^',color='r',label='10 Gy')
   b=mlines.Line2D([],[],marker='*',color='b',label='15 Gy')
   g=mlines.Line2D([],[],marker='v',color='g',label='25 Gy')
   m=mlines.Line2D([],[],marker='o',color='m',label='35 Gy')
   h=numpy.array([0,0.21,0.21,0.25,0.55,0.95])
   plt.legend(handles=[m,g,b,r,y],fancybox=True, framealpha=0.5,loc=1)
   pylab.plot(T,Atot,colors[num],TIME*60,Abs,ocolors[num])
   pylab.title('Total Absorbance')
   pylab.ylabel('Absorbance')
   pylab.xlabel('time(min)')
   #pylab.savefig('Abs.png')

   pylab.figure(2)
   plt.text(AvgDiameters[5]*(1e+9)/2-2,13.5e-7,'35 Gy',color='m')
   plt.text(AvgDiameters[4]*(1e+9)/2-2,8e-7,'25 Gy',color='g')
   plt.text(AvgDiameters[3]*(1e+9)/2-2,3.6e-7,'15 Gy',color='b')
   plt.text(AvgDiameters[2]*(1e+9)/2-2,3e-7,'10 Gy',color='r')
   plt.text(AvgDiameters[1]*(1e+9)/2-2,3e-7,'5 Gy',color='y')
   pylab.plot(Radius,S1[-1,:],str(colors[num]))
   pylab.axvline(x=AvgDiameters[num]*(1e+9)/2,ymin=h[num]-0.2,ymax=h[num],linestyle='--
',color=colors[num],linewidth=3)
   pylab.ylabel('Concentration(uM)')
   pylab.xlabel('Particle radii(nm)')
   pylab.title('Final Size Distribution')
   #pylab.savefig('Bins.png')

   pylab.figure(3)
   plt.legend(handles=[y,r,b,g,m],fancybox=True, framealpha=0.5)
   pylab.plot(T,Prec,colors[num])
```

```
pylab.title('Precursor consumption')
pylab.ylabel('Precursor Conc')
pylab.xlabel('time(min)')

out=numpy.array([N0[0],M[2,-1],Atot[-1]])
print(out)
```